Journal of Structural Biology: X 7 (2023) 100082

Contents lists available at ScienceDirect

Journal of Structural Biology: X

journal homepage: www.sciencedirect.com/journal/journal-of-structural-biology-x

Assignment of aromatic side-chain spins and characterization of their distance restraints at fast MAS

Sahil Ahlawat, Subbarao Mohana Venkata Mopidevi, Pravin P. Taware, Sreejith Raran-Kurussi, Kaustubh R. Mote, Vipin Agarwal *

Tata Institute of Fundamental Research Hyderabad, Sy. No. 36/P, Gopanpally Village, Serilingampally Mandal, Ranga Reddy District, Hyderabad 500 046, India

ARTICLE INFO

Edited by Bauke W. Dijkstra

Keywords:
Aromatic side-chain assignments
Multiple acquisitions
^{1}H–^{1}H distance restraints
Fast MAS
Solid-state NMR

ABSTRACT

The assignment of aromatic side-chain spins has always been more challenging than assigning backbone and aliphatic spins. Selective labeling combined with mutagenesis has been the approach for assigning aromatic spins. This manuscript reports a method for assigning aromatic spins in a fully protonated protein by connecting them to the backbone atoms using a low-power TOBSY sequence. The pulse sequence employs residual polarization and sequential acquisitions techniques to record H^{N}- and H^{C}-detected spectra in a single experiment. The unambiguous assignment of aromatic spins also enables the characterization of ^{1}H–^{1}H distance restraints involving aromatic spins. Broadband (RFDR) and selective (BASS-SD) recoupling sequences were used to generate H^{N}-H^{C}, H^{C}-H^{N} and H^{C}-H^{C} restraints involving the side-chain proton spins of aromatic residues. This approach has been demonstrated on a fully protonated U-[^{13}C,^{15}N] labeled GB1 sample at 95–100 kHz MAS.

Introduction

With recent improvements in probe hardware, solid-state nuclear magnetic resonance (ssNMR) at a magic angle spinning (MAS) frequency of ~100 kHz is routinely employed in several labs. Under these conditions, ^{1}H-detection allows protein characterization using sub-milligram amounts of protein (Agarwal et al., 2014). Structures of microcrystalline proteins (Agarwal et al., 2014; Andreas et al., 2016), membrane proteins (Lakomek et al., 2017; Schubeis et al., 2020), amyloids (Daskalov et al., 2021) and large protein assemblies (Lecoq et al., 2019, 2020) have been solved using ^{1}H-detection. Protein dynamics, protein–ligand and protein interactions with other biomolecules have also been studied using these methods (Ahlawat et al., 2022a; Ghassemi et al., 2022; Le Marchand et al., 2022).

Nevertheless, spectral mapping of peaks to atoms in a molecule remains the main bottleneck in these studies. The protocols for backbone assignments at fast MAS have been reported and reviewed extensively in the literature (Andreas et al., 2015; Fraga et al., 2017; Higman, 2018; Penzel et al., 2015; Sharma et al., 2020; Stanek et al., 2020; Xiang et al., 2015). Recording multiple assignment spectra are time-intensive and the experimental data suffers from instrumental instabilities (sample temperature, drifts in the magnetic field, fluctuations in magic angle settings) and possibly sample degradation. The duration of data acquisition can be significantly reduced by employing multiple acquisition approaches to acquire multiple spectra in a single experiment. The multiple acquisition experiments use various elements such as simultaneous CP (sim-CP) (Herbst et al., 2008), multiplexing (Ivchenko et al., 2003), bidirectional CP (Gopinath and Veglia, 2012a), residual polarization (Banigan and Traaseth, 2012; Gopinath and Veglia, 2012a), multiple receivers (Herbst et al., 2008; Takeda et al., 2012) and sequential and simultaneous acquisition (Bjerring et al., 2012; Gopinath and Veglia, 2012b) to record signals from multiple coherence pathways in a single experiment. However, backbone assignments are insufficient for most biomolecular studies and side-chain information is often required. Side-chain assignments have been performed by linking side-chain ^{13}C and $^{1}H^{C}$ atoms to the backbone atoms (Agarwal and Reif, 2008; Kulminskaya et al., 2015). Linking multiple ^{13}C side-chain atoms to backbone $^{13}C^{\alpha}/^{15}$N atoms requires multistep polarization transfer. The polarization transfer during first-order dipolar recoupling sequences like DREAM (dipolar recoupling enhanced by adiabatic modulation) (Verel et al., 2001) and RFDR (radio frequency driven recoupling) (Bennett et al., 1992) suffers from dipolar truncation and are ill-suited for linking multiple carbon atoms in long side-chains of Leu, Ile, Lys etc. A second-order dipolar recoupling sequence, AL FRESCO (adiabatic linearly frequency swept recoupling), shows multistep polarization transfer in the fast MAS regime but employs mixing times on the order of

* Corresponding author.
E-mail address: vipin@tifrh.res.in (V. Agarwal).

https://doi.org/10.1016/j.yjsbx.2022.100082
Received 18 August 2022; Received in revised form 18 November 2022; Accepted 27 December 2022
Available online 29 December 2022

a second (Wi and Frydman, 2020). The side-chain ^{13}C atoms have also been assigned in HET-s fibrils by recording a ^{1}H-detected 3D ^{13}C DQ-SQ (double quantum-single quantum) spectrum (Tolchard et al., 2018). The t_1 dimension encodes the DQ evolution of the two directly bonded ^{13}C spins, which is used to assign $^{1}H^{C}$ spins. The larger dispersion in the t_1 dimension results in better separation of the peaks but comes at the expense of larger spectral width in the indirect dimension.

In solution-state NMR, multistep homonuclear polarization transfer along the amino acid side-chain is efficiently achieved via scalar (J) couplings (Cavanagh et al., 2010). Scalar coupling transfer is isotropic, impervious to motions and particularly in solids, independent of crystallite orientation and MAS frequency. Scalar couplings are approximately two-orders of magnitude weaker than dipolar couplings and require effective proton decoupling for efficient transfer. At fast MAS, J-couplings-based transfer can be achieved by solution-state sequences such as WALTZ-16 (Kulminskaya et al., 2016; Stanek et al., 2016) or equivalent solid-state TOBSY (total through bond correlation spectroscopy) sequences (Baldus and Meier, 1996; Hardy et al., 2003; Hardy et al., 2001). Symmetry sequences enable efficient scalar coupling transfer despite the two-order smaller magnitude of the interaction (Levitt, 2007). Recently, $C9^{1}_{39}$ and $C9^{1}_{48}$ symmetry sequences were shown to provide high polarization (~70–80 %) transfer efficiencies at fast MAS while employing low rf fields (Tan et al., 2018). These symmetry numbers also efficiently decouple heteronuclear dipolar and scalar coupling interactions, thereby eliminating the need for ^{1}H decoupling during mixing, especially in the fast MAS regime. At fast MAS, these TOBSY sequences show better polarization transfer efficiency between aliphatic ^{13}C side-chain spins than other solution-state sequences such as WALTZ-16 (Paluch et al., 2022). The pulse sequences utilizing J-based transfers have been used to acquire 3D, 4D or 5D spectra for assigning side-chain spins (Klein et al., 2022a; Klein et al., 2022b; Schubeis et al., 2021; Stanek et al., 2016). Alternatively, INADEQUATE (incredible natural abundance double quantum transfer experiment) (Lesage et al., 1997; Lesage et al., 1999), UC2QF-COSY (uniform-sign cross-peak double-quantum-filtered correlation spectroscopy) (Mueller et al., 2002; Olsen et al., 2003) and CTUC-COSY (constant-time uniform cross-peak correlation spectroscopy) (Chen et al., 2006) have also been used to link one/two bond separated side-chain atoms but require long transverse coherences.

Although these developments have resulted in the routine assignment of aliphatic side-chains, the assignment of aromatic side-chains remains an issue. Selective labeling/unlabeling and mutagenesis are still the most commonly used methods for aromatic side-chain assignments (Ghosh and Rienstra, 2017; Kainosho et al., 2006; Shcherbakov and Hong, 2018; Torizawa et al., 2005). Side-chain $^{13}C^{aro}$ spins have higher deshielding resulting in distinct chemical shifts (~110–140 ppm) compared to aliphatic spins (10–70 ppm). Large chemical shift anisotropy (CSA) and complex dynamics in aromatic side-chains can hinder efficient polarization transfer via dipolar coupling-based sequences and significantly limit the possibility of assignment. This fact is evident in the BMRB database, with an exceedingly low number of assignments deposited for the aromatic side-chains. There are few reports of aromatic side-chain assignments in small proteins by employing WALTZ-16, DQ-SQ and AL-FRESCO sequences (Andreas et al., 2016; Tolchard et al., 2018; Wi and Frydman, 2020). Generally, only the aromatic spins with distinct chemical shifts are assigned with these sequences. In a few cases, the complete side-chain assignment was possible because of the single occurrence of a particular aromatic residue in the protein sequence. An efficient $^{13}C^{aro} \rightarrow {}^{13}C^{\alpha}$ polarization transfer sequence is required to assign the aromatic spins. The CN^{ν}_{n} symmetry-based TOBSY sequences are well suited for this purpose and are explored for the aromatic side-chain spins assignment in this manuscript. Obtaining spatial contacts for the aromatic spins has also remained challenging but can be extremely useful in structural applications. In addition to proposing a strategy to obtain assignments of aromatic residues, we also propose methods for observing a large density of spatial contacts involving aromatic proton spins.

In this study, we show the assignment of the aromatic side-chain atoms using $C9^{1}_{48}$-based TOBSY mixing on U-[^{13}C,^{15}N] labeled GB1 at ~95.23 kHz MAS. The aromatic side-chain $^{1}H/^{13}C$ spins are correlated to the backbone spin pairs, such as $C^{\alpha}H^{\alpha}$ and NH and side-chain spins, such as $C^{\beta}H^{\beta}$. These 2D $C^{\alpha}H^{\alpha}$, NH and $C^{\beta}H^{\beta}$ spin-pairs show the largest dispersion and are routinely used as high-resolution 2D-fingerprint spectra in multidimensional solid-state NMR spectroscopy. Multispin simulations of aromatic residues were used to assess the performance of WALTZ-16, $C9^{1}_{39}$ and $C9^{1}_{48}$ symmetry sequences for $^{13}C^{aro} \rightarrow {}^{13}C^{\alpha}/{}^{13}C^{\beta}$ transfer. The simultaneously acquired $(H)C^{aro}NH^{N}$-TOBSY and $(H)C^{aro}CH^{C}$-TOBSY spectra link the aromatic side-chain atoms to the backbone ^{15}N, $^{1}H^{N}$, $^{13}C^{\alpha}$ and $^{1}H^{\alpha}$ atoms. The $^{1}H^{aro}$ spins can also be independently assigned from the $(H)C^{aro}CH^{C}$-TOBSY spectrum. The ^{1}H–^{1}H restraints for aromatic residues were obtained using the broadband recoupling sequence RFDR and selective recoupling sequence BASS-SD (Band-selective spectral spin diffusion) (Jain et al., 2017). These two mixing sequences were used in a pulse sequence that combines four experiments to generate $H^{N} \leftrightarrow H^{N}$, $H^{N} \leftrightarrow H^{aro}$ and $H^{aro} \leftrightarrow H^{aro}$ distance restraints. In the case of GB1, the aromatic restraints provide important contacts in the hydrophobic core and assist in arranging the α-helix and β-sheets in the 3D structure.

Result and discussion

The strategy of linking aromatic side-chain spins to backbone atoms is analogous to that employed in the aliphatic side-chain assignment (Agarwal and Reif, 2008; Kulminskaya et al., 2015). Typically, 3D/4D $HCNH^{N}$ and $HCCH^{C}$ spectra have been used to assign the aliphatic side-chains. The same 3D spectra can be used to assign aromatic spins with an efficient multistep homonuclear polarization transfer sequence such that aromatic spins are linked to $^{13}C^{\alpha}/{}^{13}C^{\beta}$ spins. Acquiring a single experiment for both aliphatic and aromatic side-chain spins is possible but suffers from practical challenges. The large differences in the isotropic chemical shifts, CSAs and scalar couplings of aliphatic and aromatic side-chain carbon atoms result in marginally different optimum conditions for ^{1}H–^{13}C CP and multi-bond ^{13}C–^{13}C scalar coupling transfers. In addition, the need for acquiring two indirect dimensions with large spectral widths can be avoided in separate experiments. Anyways, the significant difference in the signal-to-noise observed for aromatic and aliphatic spins requires different extents of signal averaging. A pulse sequence linking only aromatic side chains to backbone atoms can also be employed for spectral editing and identifying backbone peaks of aromatic residues in 2D HC and HN heteronuclear correlation spectra. An independent 3D experiment optimized only for aromatic residue correlations is discussed in the next section.

Pulse sequence for aromatic side-chain assignment

The pulse sequence for aromatic side-chain assignment is largely similar to the reported 3D $(H)C(C^{\alpha})NH^{N}$ sequence used to assign side-chain spins in the perdeuterated and fully protonated samples (Kulminskaya et al., 2016). However, two key differences from the previous report are the selection of only aromatic signals and the employment of $C9^{1}_{48}$ symmetry sequence for scalar transfer. Linking side-chains to the peaks in the NH^{N} plane is preferred over the $C^{\alpha}H^{\alpha}$ plane because of the larger dispersion of ^{1}H-^{15}N peaks. As previously reported, the $^{13}C^{\alpha}$-^{15}N SPECIFIC-CP block (employed for heteronuclear polarization transfer in the 3D $(H)CNH^{N}$ pulse sequence) transfers only ~30 % of the $^{13}C^{\alpha}$ polarization to the ^{15}N spins (Loening et al., 2012; Nielsen et al., 2013). This implies that after $^{13}C^{\alpha}$-^{15}N SPECIFIC-CP, ~70 % of the initial polarization on $^{13}C^{\alpha}$ and ~90–100 % of polarization on the other ^{13}C atoms is intact and can be utilized to record a 3D $(H)CCH^{C}$-TOBSY spectrum.

Fig. 1A shows the pulse sequence to simultaneously record 3D (H)

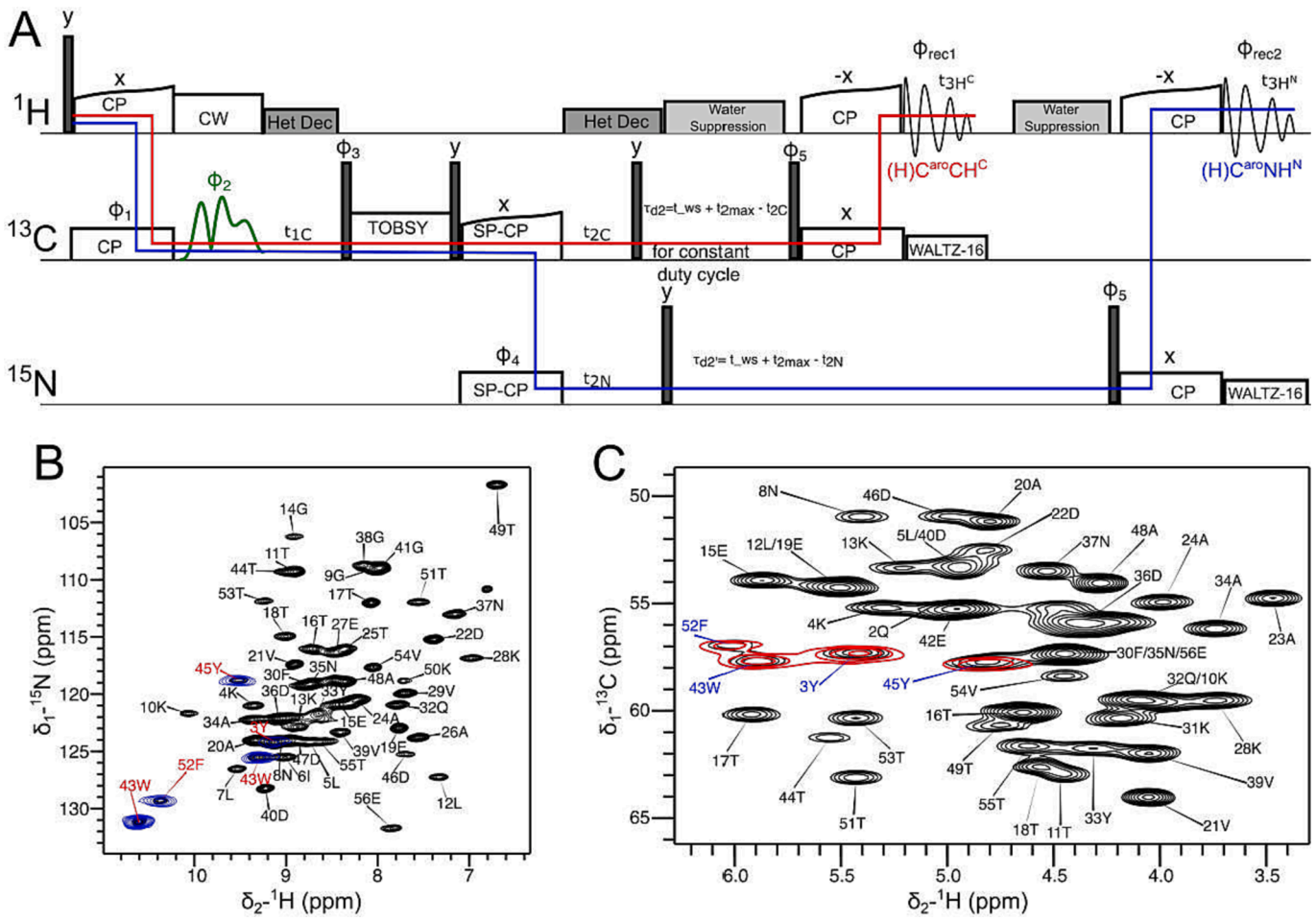

Fig. 1. (A) The pulse sequence for the aromatic side-chain assignment. The polarization transfer pathways for (H)C^{aro}CH^{C}-TOBSY and (H)C^{aro}NH^{N}-TOBSY spectra are shown in red and blue, respectively. The pulse sequence stores H^{C}- and H^{N}-detected spectra separately so multiplexing is not required. The individual spectrum is obtained by separating the even and odd FIDs along the t_1 dimension. The SLAP (Solvent suppression using adiabatic pulses) sequence is used for water suppression (Matsunaga et al., 2021). The rCW^{ApA} sequence was used for ^{1}H decoupling while WALTZ-16 heteronuclear decoupling was used during ^{1}H detection. The phase cycling for the pulse sequence is: Φ_1 = x, −x; Φ_2 = x, x, y, y; Φ_3 = y; Φ_4 = x, x, −x, −x; Φ_5 = −y, −y, −y, −y, y, y, y, y; Φ_{rec1} = x, −x, −x, x, −x, x, x, −x and Φ_{rec2} = −x, x, −x, x, x, −x, x, −x. (B, C) The aromatic residues filtered 2D NH^{N} (blue) and C$^{\alpha}$H$^{\alpha}$ (red) heteronuclear correlation spectra overlaid with the unfiltered heteronuclear correlation spectra. The filtered spectra were recorded with the pulse sequence (A) without t_{1C} evolution as pseudo-3D. (B) The overlay of the 2D (H)(C^{aro})NH^{N}-TOBSY spectrum (blue) with the 2D NH^{N}-HSQC spectrum (black). The 2D (H)(C^{aro})NH^{N}-TOBSY spectrum has five peaks belonging to 4 residues (3Y, 43W, 45Y, 52F and 43W$^{\varepsilon1}$) are labeled in red. (C) The overlay of the 2D (H)(C^{aro})CH^{C}-TOBSY spectrum (red) with the 2D C$^{\alpha}$H$^{\alpha}$-HSQC spectrum (black). The 2D (H)(C^{aro})CH^{C}-TOBSY spectrum has four peaks belonging to (3Y, 43W, 45Y and 52F), which are labeled in blue. The peaks of 30F and 33Y are not visible in both spectra. The complete overlay of (H)(C^{aro})CH^{C}-TOBSY spectrum (red) with CH^{C}-HSQC (black) is shown in Fig. S2. (For interpretation of the references to color in this figure legend, the reader is referred to the web version of this article.)

C^{aro}CH^{C}-TOBSY and (H)C^{aro}NH^{N}-TOBSY. A 180° selective pulse after the ^{1}H–^{13}C CP (shown in green in Fig. 1A) combined with two-step phase cycling retains all the aromatic ^{13}C magnetization, while the non-aromatic ^{13}C magnetization is cancelled out after adding two scans. The ^{13}C^{aro} resonances are encoded in the t_1 dimension. The TOBSY block enables homonuclear ^{13}C polarization transfer amongst the directly bonded ^{13}C atoms. In our case, after the ^{13}C$^{\alpha}$-^{15}N SPECIFIC-CP block, ~73 % of the initial ^{13}C$^{\alpha}$ magnetization remains on ^{13}C$^{\alpha}$, implying that at best ~27 % of the initial magnetization is transferred to ^{15}N spins. The other aliphatic carbons retain ~90–95 % of the initial magnetization. In the second evolution period (t_2), the polarization on ^{15}N and the residual polarization on ^{13}C atoms evolve simultaneously (t_{2N} and t_{2C}). The π/2-pulses applied on ^{13}C and ^{15}N channels store the magnetization along the z-direction. The τ_{d2} and $\tau_{d2'}$ are the delays for maintaining a constant duty cycle after t_{2C} and t_{2N}, respectively. The water suppression block minimizes the solvent signals and a subsequent π/2-pulse followed by ^{13}C–^{1}H back CP enables the detection of ^{1}H^{C} magnetization (red pathway in Fig. 1A). For this entire duration, ^{15}N magnetization is stored along the z-direction. H^{N} polarization is detected after CP from ^{15}N following a π/2-pulse after applying the second water suppression block (blue pathway in Fig. 1A). H^{C} polarization is detected before H^{N} because of the shorter carbon T_1. The τ_{d2} and $\tau_{d2'}$ delays, in addition to maintaining a constant duty cycle, also allow arbitrary spectral widths and independent evolution blocks for the ^{15}N and ^{13}C spins. The pulse sequence stores the H^{C} and H^{N} signals in an interleaved fashion (See supplementary information for the pulse program code implemented on Bruker Spectrometers). The first FID encodes signals from the (H)C^{aro}CH^{C}-TOBSY pathway (depicted by a red line in Fig. 1A), while the second FID encodes signals from the (H)C^{aro}NH^{N}-TOBSY pathway (depicted by the blue line in Fig. 1A). The FIDs from the (H)C^{aro}CH^{C}-TOBSY pathway are stored as odd FIDs, while the FIDs from the (H)C^{aro}NH^{N}-TOBSY pathway are stored as even FIDs. Therefore, the 3D dataset has a factor of two larger t_1 points than the actual size of the individual spectrum.

TOBSY block was independently optimized for ^{13}C^{aro} → ^{13}C$^{\alpha}$ transfer using a 1D (H)C^{aro}CH^{C}-TOBSY spectrum. The optimum TOBSY ($C9^{1}_{48}$)

mixing time was 20 ms with ^{13}C carrier frequency at 90 ppm (See Table S3). The offset, rf amplitude and mixing time of the TOBSY block were optimized to maximize the intensity in the H^{α} region (Fig. S1). The pulse sequence (Fig. 1A) is also an aromatic residue filtering experiment. The 2D spectra recorded without t_1 evolution can also be used to identify the backbone peaks of aromatic residues in the 2D ^{15}N-$^{1}H^{N}$ and $^{13}C^{\alpha}$-$^{1}H^{\alpha}$ heteronuclear correlation spectra (Fig. 1B, C and Fig. S2).

Resonance assignment from the (H)$C^{aro}NH^{N}$-TOBSY and (H)$C^{aro}CH^{C}$-TOBSY spectra

The H^{N}-detected spectrum, (H)$C^{aro}NH^{N}$-TOBSY, generally has better resolution because of the NH plane, while the H^{C}-detected spectrum, (H)$C^{aro}CH^{C}$-TOBSY, has higher sensitivity. In the (H)$C^{aro}NH^{N}$-TOBSY spectrum (Fig. 2; blue spectrum), $^{13}C^{aro}$ side-chain atoms in the F_1 dimension are linked to peaks in the 2D ^{1}H-^{15}N spectra. In contrast, in the (H)$C^{aro}CH^{C}$-TOBSY spectrum (Fig. 2; red spectrum), the $^{13}C^{aro}$ side-chain atoms in the F_1 dimension are linked to peaks in the 2D ^{1}H–^{13}C CP-based one-bond heteronuclear correlation plane. The backbone ^{15}N, $^{1}H^{N}$, $^{13}C^{\alpha}$ and $^{1}H^{\alpha}$ chemical shifts must be assigned before assigning side-chain aromatic atoms. These backbone chemical shifts were assigned using the multi-acquisition approach and the backbone walk is shown in Fig. S3 of the supplementary information (Sharma et al., 2020).

The $^{13}C^{aro}$ and $^{1}H^{aro}$ side-chain peaks were assigned from the 3D (H)$C^{aro}NH^{N}$-TOBSY and 3D (H)$C^{aro}CH^{C}$-TOBSY spectra, respectively. In the 3D (H)$C^{aro}NH^{N}$-TOBSY spectrum, the $^{13}C^{aro}$ peaks were assigned in the F_1 dimension (dotted horizontal lines in Fig. 2A and B). The 3D (H)$C^{aro}CH^{C}$-TOBSY spectrum verifies the assigned peak using the $C^{\alpha}H^{\alpha}$ plane. The $^{1}H^{aro}$ chemical shifts were assigned from the (H)$C^{aro}CH^{C}$-TOBSY spectrum. Using the chemical shifts of an assigned $^{13}C^{aro}$ atom, the $^{1}H^{aro}$ (dotted vertical lines in Fig. 2A and B) spins were identified and assigned. Fig. 2A shows the strips for aromatic side-chain assignments of 43W. Using the ^{15}N and $^{1}H^{N}$ chemical shifts, the $C^{\delta1}$ and $C^{\varepsilon3}$/$C^{\zeta3}$ peaks are assigned in the (H)$C^{aro}NH^{N}$-TOBSY spectrum (the blue strip in Fig. 2A). In the (H)$C^{aro}CH^{C}$-TOBSY spectrum, the $C^{\alpha}H^{\alpha}$ peak in the HSQC plane (F_2-F_3) is linked to $C^{\delta1}$ and $C^{\varepsilon3}$/$C^{\zeta3}$ in F_1. Peaks for the entire

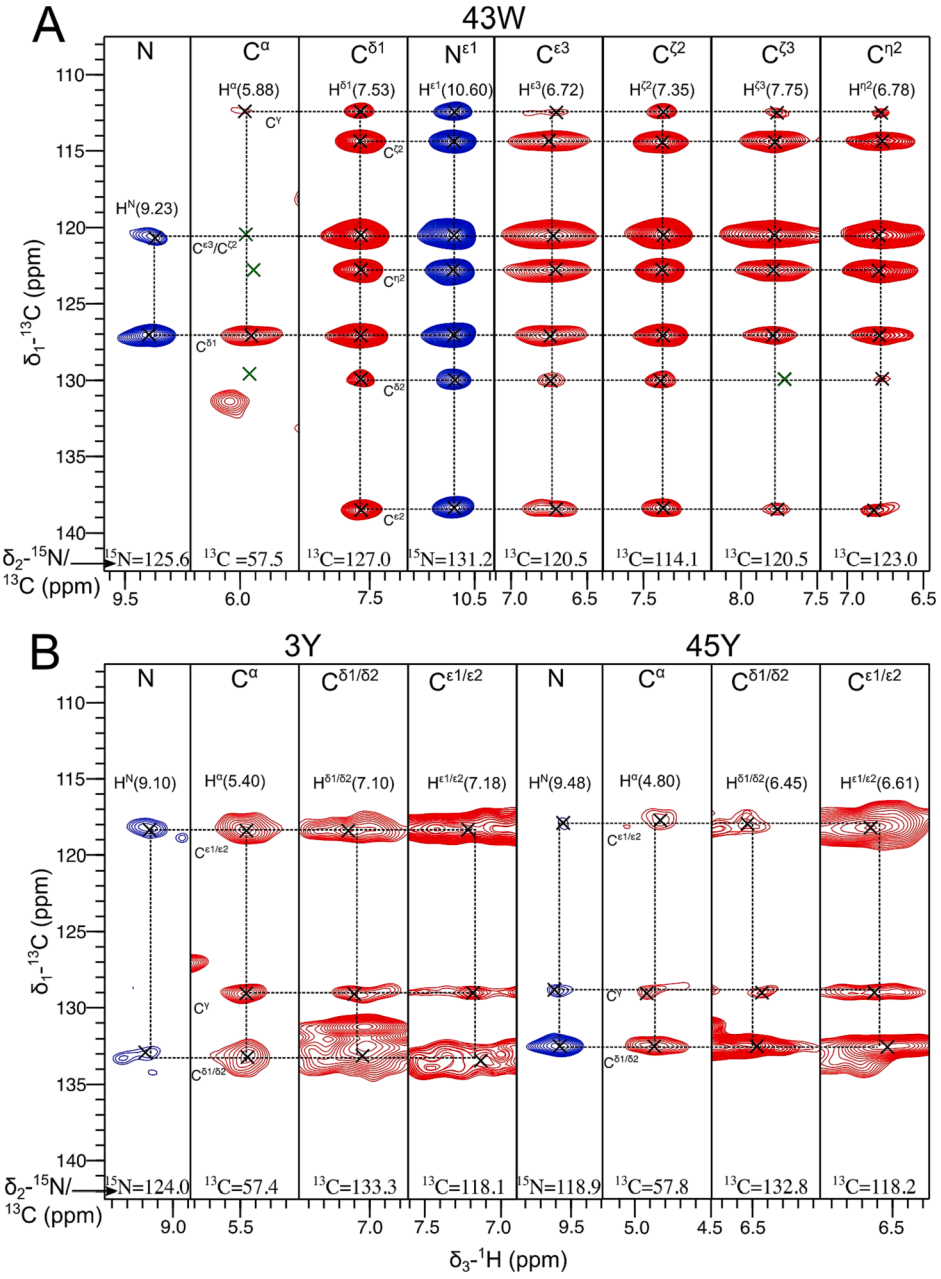

Fig. 2. The F_1-F_3 strips of the spectra obtained from the pulse sequence in Fig. 1A for the aromatic side-chain assignment. The 3D (H)$C^{aro}NH^{N}$-TOBSY spectrum is colored blue and the 3D (H)$C^{aro}CH^{C}$-TOBSY spectrum is colored red. The F_1-F_3 strips for residues (A) 43W, (B) 3Y and 45Y are shown. The $^{13}C^{aro}$ side-chain atoms are assigned from the F_1 dimension of the 3D (H)$C^{aro}NH^{N}$-TOBSY spectrum (blue) using the NH^{N} plane. The side-chain peaks are connected with the vertical dotted line in the 3D (H)$C^{aro}NH^{N}$-TOBSY spectrum. The assigned $^{13}C^{aro}$ atoms are used to assign the $^{1}H^{aro}$ chemical shifts in the 3D (H)$C^{aro}CH^{C}$-TOBSY spectrum (red). The F_1-F_3 plane at the $^{13}C^{aro}$ chemical shifts of side-chain atoms provides the assignment of $^{1}H^{C}$ atoms. The horizontal dotted line connects the $^{13}C^{aro}$ side-chain atoms between the strips of (H)$C^{aro}NH^{N}$-TOBSY (blue) and (H)$C^{aro}CH^{C}$-TOBSY (red) spectra. The vertical dotted lines assign $^{1}H^{C}$ atoms in the red strips. The green cross (x) indicates the peaks with lower intensity. These peaks are visible at lower contour levels and are shown in Fig. S5B. The experiment was recorded on U-[^{13}C,^{15}N]-GB1 on a 700 MHz spectrometer at 95.238 kHz MAS. (For interpretation of the references to color in this figure legend, the reader is referred to the web version of this article.)

aromatic side-chain of 43W are correlated to the $N^{\varepsilon1}$-$H^{\varepsilon1}$ in the (H)C^{ar}-$^{o}NH^{N}$-TOBSY spectrum (the blue strip in Fig. 2A). From the (H)$C^{aro}CH^{C}$-TOBSY spectrum, the $^{13}C^{aro}$ chemical shifts in the F_2 dimension were used to assign $^{1}H^{aro}$ spins. This approach assigned all the $^{13}C^{aro}$ and $^{1}H^{aro}$ peaks for the 43W (Fig. 2A). The aromatic spins for 3Y and 45Y were also similarly assigned (Fig. 2B). The C^{γ}, $C^{\delta1/\delta2}$ and $C^{\varepsilon2/\varepsilon3}$ along with $H^{\delta1/\delta2}$ and $H^{\varepsilon1/\varepsilon2}$ spins, were assigned for 3Y and 45Y residues. The peaks corresponding to C^{ζ} and H^{η} spins were not observed in both spectra. The H^{η} atom is not directly bonded to C^{ζ} so its peak will not be visible. For 52F, two peaks around 131 and 140 ppm are visible (Fig. S4). The peak at 140 ppm belongs to C^{γ} while the peak at 131 ppm could belong to either $C^{\delta1/\delta2}$(~131.5 ppm), $C^{\varepsilon1/\varepsilon2}$ (130.7 ppm) and C^{ζ} (~129.2 ppm) or all of the atoms. The parentheses report the average chemical shift of these atoms from the BMRB database with a standard deviation of 1.2–1.4 ppm. The poor chemical shift dispersion of the $C^{\delta1/\delta2}$, $C^{\varepsilon1/\varepsilon2}$ and C^{ζ} side-chain atoms can be remedied by selective labeling (Gauto et al., 2022; Gauto et al., 2019; Teilum et al., 2006). Except for the –OH group, the F and Y residues have a similar side-chain architecture, so we expect polarization transfer profiles along the side-chain atoms to be similar.

In principle from the 3D (H)$C^{aro}CH^{C}$-TOBSY, the C^{β}-H^{β} plane can also be used to assign aromatic spins. The aromatic residue assignments are listed in Table S1 in the supporting information. The strips for the $^{13}C^{\beta}$ chemical shifts are shown in Fig. S5A. Numerical simulations (shown below) indicate that in the best-case scenario, ~10 % polarization is transferred from aromatic carbons to C^{α} and C^{β} spins. We do not observe the $C^{\alpha}H^{\alpha}$ and NH^{N} peaks for 30F and 33Y in either the (H)$C^{aro}CH^{C}$-TOBSY or the (H)$C^{aro}NH^{N}$-TOBSY spectra, i.e., when the initial magnetization is on the aromatic spins. However, we observe the $C^{\alpha}H^{\alpha}$ and NH^{N} peaks for the 30F and 33Y residues in the regular 2D heteronuclear correlation spectra (black spectrum in Fig. 1B and C). Both residues are present in the α-helix region and face the β3-strand. Previously, it has been shown that the residues in the α-helix facing the β-strands have large to moderate amplitude motions (Shi and Rienstra, 2016). Motional broadening or poor ^{1}H–^{13}C dipolar transfer in the aromatic side-chain could explain the absence of these residues in the spectra.

The pulse sequence in Fig. 1A can also be used to acquire spectra for the assignment of aliphatic side-chain spins. The spectra are acquired without a selective pulse and TOBSY is optimized for transfer within the aliphatic region. The strips for the 3D (H)$C^{ali}NH^{N}$-TOBSY (blue) and 3D (H)$C^{ali}C^{ali}H^{ali}$-TOBSY (red) spectra are shown in Fig. S6.

TOBSY transfer efficiency in numerical simulations

Numerical simulations were used to assess the transfer efficiency from $^{13}C^{aro} \rightarrow {}^{13}C^{\alpha}$ spins with various scalar coupling transfer sequences such as $C9^{1}_{39}$, $C9^{1}_{48}$ and WALTZ-16. SIMPSON simulations (Bak et al., 2000; Tošner et al., 2014) were performed for histidine, phenylalanine and tyrosine spin systems and details of the spin system are reported in Figs. S7 and S8 in supplementary information. At fast MAS, the detrimental effects of protons during the TOBSY irradiation are minimized (Tan et al., 2018; Paluch et al., 2022). Hence, protons were omitted from the spin systems to reduce the computational time. For the histidine spin system, the initial polarization was selected to be on the C^{γ} and $C^{\delta2}$ aromatic spins. In contrast, for the phenylalanine and tyrosine residues, the initial polarization was limited to C^{γ}, $C^{\delta1}$ and $C^{\varepsilon1}$ spins. The initial polarization was limited to spins that correlated to $^{13}C^{\alpha}$ spins in the 3D experimental spectra. Simulations were performed at 95.238 kHz MAS frequency and a static field of 16.44 T. All other simulation parameters are reported in the supplementary information. Points in the simulated magnetization buildup curves were acquired after 39, 48 and 96 rotor periods for $C9^{1}_{39}$, $C9^{1}_{48}$ and WALTZ-16 sequences, respectively.

Fig. 3 shows symmetry sequences have better transfer efficiencies than WALTZ-16 with $C9^{1}_{48}$ TOBSY being the best. The optimum duration for $^{13}C^{aro} \rightarrow {}^{13}C^{\alpha}$ scalar coupling transfer is ~20 ms and is similar to experimentally optimized duration and was also used in recording 3D spectra (Table S3 in supplementary information). The transfer efficiencies from aromatic carbons to $^{13}C^{\alpha}$ and $^{13}C^{\beta}$ atoms with 20 ms of $C9^{1}_{48}$ TOBSY mixing is ~9–10 % for phenylalanine and tyrosine residue, while for histidine, the same is higher due to a shorter spin-system. The detailed transfer efficiencies are summarized in Table S2 in supplementary information.

^{1}H–^{1}H restraints involving aromatic protons

High-resolution NMR structure calculation requires a large set of distance restraints (~15 per residue) (Russell et al., 2019). The general approach is to record multiple second-order dipolar recoupled spectra. The observed peaks are evidence of spatial proximity within the limit of upper distance restraints determined by the details of the recoupling sequence and mixing time (Manolikas et al., 2008). Both broadband (RFDR) and selective recoupling sequences such as BASS-SD (band-selective spectral spin-diffusion), SERP (selective recoupling of protons) and MODIST (modest offset difference internuclear selective transfer)

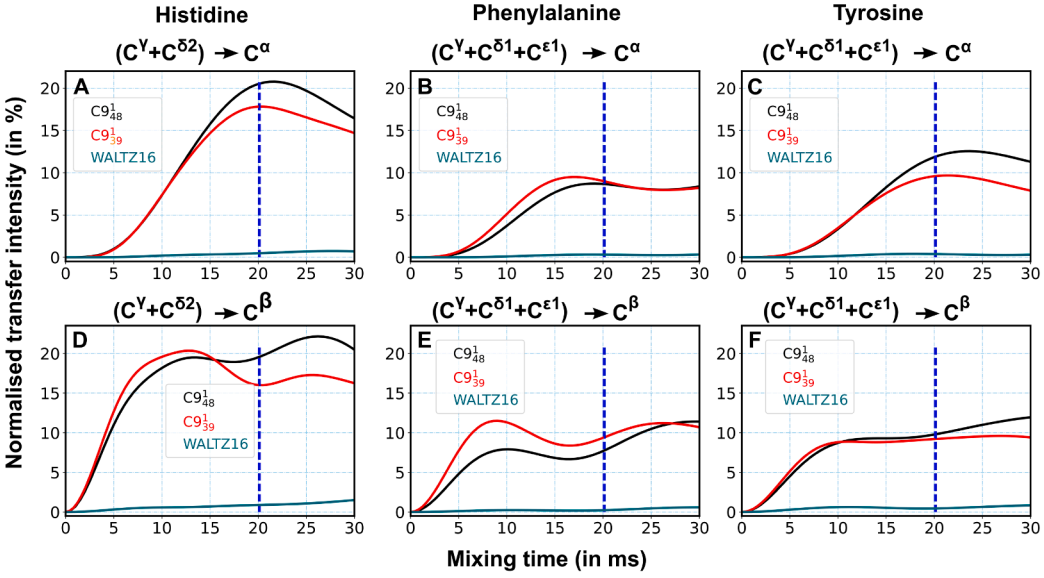

Fig. 3. Simulated polarization transfers build up from side-chain aromatic atoms of histidine (A and D), phenylalanine (B and E) and tyrosine (C and F) residues to $^{13}C^{\alpha}$ atom (A-C) and $^{13}C^{\beta}$ atoms (D-F). Simulations are performed at 95.238 kHz MAS at a static field of 16.4 T (700 MHz) using $C9^{1}_{48}$ (black), $C9^{1}_{39}$ (red) and WALTZ-16 (teal) sequences, respectively. The y-axis is normalized with the cumulative initial magnetization on the aromatic atoms. The dotted vertical blue line indicates the transfer intensity at 20 ms of mixing time. The polarization transfer efficiencies from individual atoms to other atoms for the three aromatic residues are shown in supplementary information (Fig. S6). (For interpretation of the references to color in this figure legend, the reader is referred to the web version of this article.)

have been used to observe $^{1}H–^{1}H$ spatial correlations interpreted as structural restraints in the limit of upper distances (Bennett et al., 1992; Andreas et al., 2016; Jain et al., 2017; Duong et al., 2018; Potnuru et al., 2020; Nimerovsky et al., 2022). The lack of aromatic assignment has limited the engagement of aromatic protons as structural restraints (Klein et al., 2022b). After the complete ^{1}H and ^{13}C assignment of aromatic side-chain spins in the previous section, the restraints involving aromatic spins can be observed and assigned.

Ideally, four experiments, (H)N(H^N)(H^N)NH^N, (H)N(H^N)(H^C)CH^C, (H)C(H^C)(H^N)NH^N and (H)C(H^C)(H^C)CH^C are required to generate a comprehensive of H^N-H^N, H^N-H^C, H^C-H^N and H^C-H^C distance restraints. We previously demonstrated that these four experiments could be combined into a single experiment that generates four spectra for the duration required to record one H^C-H^C restraint spectrum (Ahlawat et al., 2022b). We refer to this pulse sequence as a 4X-restraint experiment, as the four spectra encode four different restraints. Here, we use the 4X-restraint pulse sequence to map out $^{1}H–^{1}H$ restraints involving aromatic residues: H^N-H^N, H^N-H^{aro}, H^{aro}-H^N and H^{aro}-H^{aro}. We recorded two independent 4X-restraint spectra, one with a broadband (RFDR) recoupling and the second with a selective recoupling (BASS-SD) to generate $^{1}H–^{1}H$ aromatic restraints. This also allowed us to evaluate the performance of broadband and selective recoupling sequence in mapping out restraints involving aromatic spins.

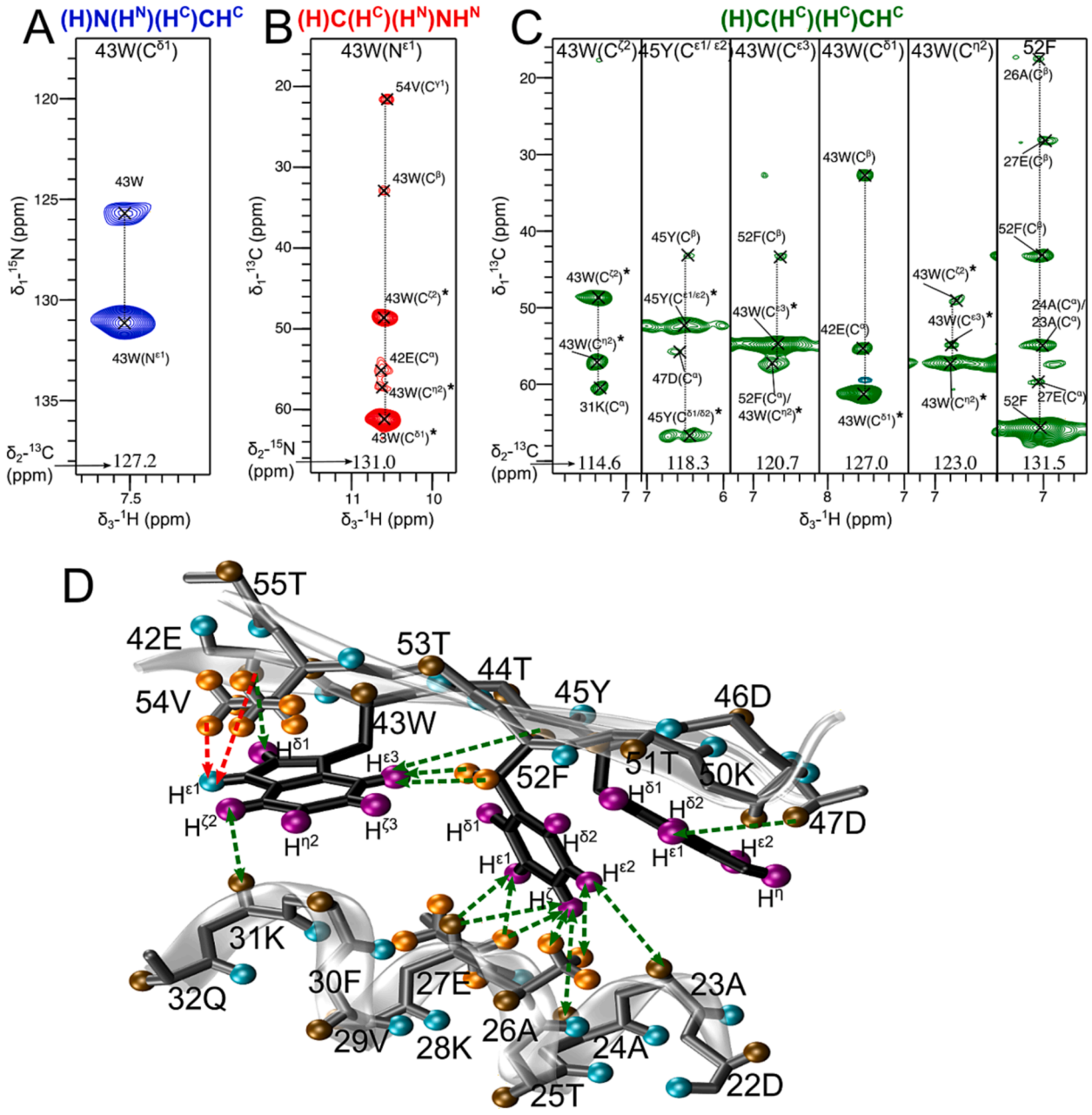

Fig. 4. The F_1-F_3 strips from the (A) (H)N(H^N)(H^C)CH^C (blue), (B) (H)C(H^C)(H^N)NH^N (red) and (C) (H)C(H^C)(H^C)CH^C (green) spectra highlight the H^N-H^{aro}, H^{aro}-H^N and H^{aro}-H^{aro} restraints for aromatic residues. The restraints spectra were acquired with the 4X-restraint pulse sequence using 920 μs of RFDR mixing. The peaks in the aromatic region were folded in the spectrum, subsequently unfolded during processing for assigning cross-peak, and marked with an asterisk (*). (D) The experimentally observed restraints between α-helix and β-sheets were plotted on the structure of GB1 (PDB: 2QMT). Only the inter-residue contacts are plotted in the figure. The H^N atoms are colored in cyan, H^{α} in brown, H^{ali} in orange and H^{aro} in purple. The H^{ali} atoms are shown for only those residues for which aromatic contacts are observed. The arrowhead indicates the direction of the transfer and the double-headed arrows are used to show contacts with two-cross peaks. (For interpretation of the references to color in this figure legend, the reader is referred to the web version of this article.)

H^N-H^{aro}, H^{aro}-H^N and H^{aro}-H^C restraints observed with RFDR mixing

RFDR is a broadband recoupling that recouples the entire proton bath, including the aromatic residues, so a selective pulse on aromatic spins is not required. Without the selective pulse, the ^{13}C spectral width is around 140 ppm (including the aliphatic and aromatic side-chain). The spectra were recorded by folding the $^{13}C^{aro}$ peaks. The distinct aromatic proton chemical shifts assist in unfolding the aromatic peaks. The restraints obtained for aliphatic protons are shown in Fig. S9 and are not explicitly discussed here.

In the (H)N(H^N)(H^C)CH^C (blue) and (H)C(H^C)(H^N)NH^N (red) spectra (Fig. 4A and B), the contacts are observed only for the 43W($H^{\varepsilon1}$) and 43W($H^{\delta1}$). A long-range 3.2 Å contact between 54V($H^{\gamma2}$)-43 W($H^{\varepsilon1}$) is visible in the (H)C(H^C)(H^N)NH^N (red) spectrum (Fig. 4B). The (H)C(H^C)(H^C)CH^C (green) spectrum (Fig. 4C) has both intra- and inter-residue contacts. The inter-residue contacts are long-range in the upper distance limit of 4–4.5 Å. The observed long-range contacts are 43W($H^{\zeta2}$)-31K(H^{α}), 43W($H^{\varepsilon3}$)-52F(H^{α}), 43W($H^{\varepsilon3}$)-52F(H^{β}), 52F(H^{aro})-26A(H^{β}), 52F(H^{aro})-24A(H^{α}), 52F(H^{aro})-23A(H^{α}), 52F(H^{aro})-27E(H^{α}) and 52F (H^{aro})-27E(H^{β}). These contacts are plotted on the structure of GB1 (Fig. 4D). Most of the observed contacts are between aromatic side-chain residues attached to the β-sheets and the aliphatic side-chain protons in the α-helix that together form the hydrophobic core in the case of GB1. Identifying several spatially proximal aromatic and aliphatic side-chain protons should help restrain the hydrophobic core of GB1.

H^N-H^{aro}, H^{aro}-H^N and H^{aro}-H^{aro} restraints observed with BASS-SD

In contrast to broadband ^1H–^1H recoupling sequences, selective recoupling sequences have been shown to provide cross-peaks with better intensities and long-range contacts in the case of proteins (Duong et al., 2020; Jain et al., 2017; Zhang et al., 2020). BASS-SD recoupling is a low-power sequence tailored to recouple a subset of proton spins in fully protonated molecules. The amide and aromatic protons have a similar chemical shift range; therefore, BASS-SD recoupling is ideally suited to generate H^N-H^{aro}, H^{aro}-H^N and H^{aro}-H^{aro} restraints.

The 4X-restraint experiment was recorded with BASS-SD mixing. In the ^{13}C dimension, the $^{13}C^{aro}$ spins were selected by employing the selective pulse (Q3; Gaussian Cascade) (Emsley and Bodenhausen, 1992). Experimentally, BASS-SD mixing was optimized to maximize $H^{aro} \rightarrow H^N$ transfer in the 2D (H)C^{aro}(H^{aro})-H spectrum. The optimum BASS-SD condition for $H^N \leftrightarrow H^{aro}$ transfer was a 6 ms tangential spin lock pulse with variable rf amplitude of 3.77–5.66 kHz at the carrier frequency of 8.15 ppm. A detailed list of experimental parameters is provided in the supplementary infomration (Table S3). The four spectra obtained by employing BASS-SD recoupling in the 4X-restraint pulse sequence are (H)N(H^N)(H^N)NH^N, (H)N(H^N)(H^{aro})$C^{aro}H^{aro}$, (H)C^{aro}(H^{aro})(H^N)NH^N and (H)C^{aro}(H^{aro})(H^{aro})$C^{aro}H^{aro}$. The (H)N(H^N)(H^N)NH^N spectrum gives only H^N-H^N restraints and has been discussed previously in literature for both BASS-SD and its variant (Jain et al., 2017; Ahlawat et al., 2022b). We do not further discuss H^N-H^N restraints in this manuscript because no aromatic side-chain spins are involved. The other three relevant spectra (H)N(H^N)(H^{aro})$C^{aro}H^{aro}$ (blue), (H)C^{aro}(H^{aro})(H^N)NH^N (red) and (H)

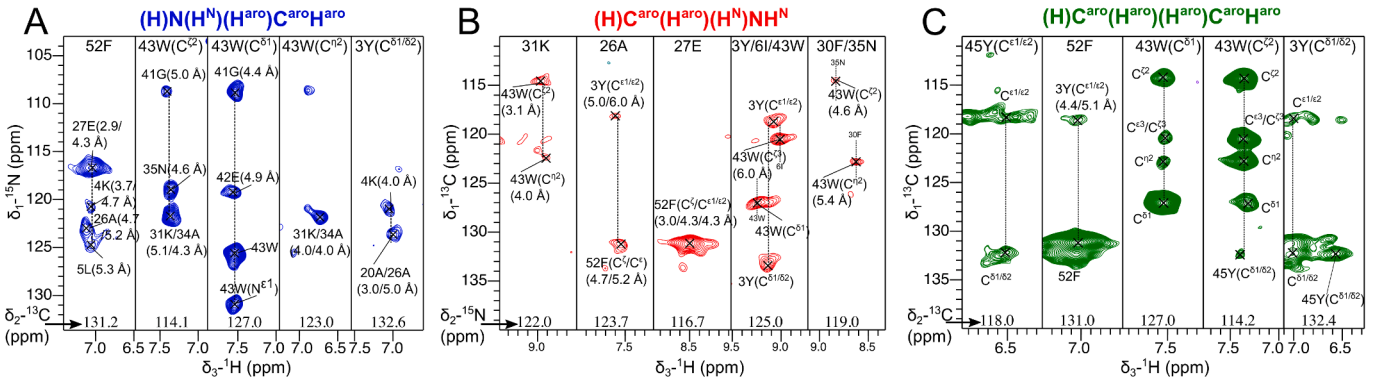

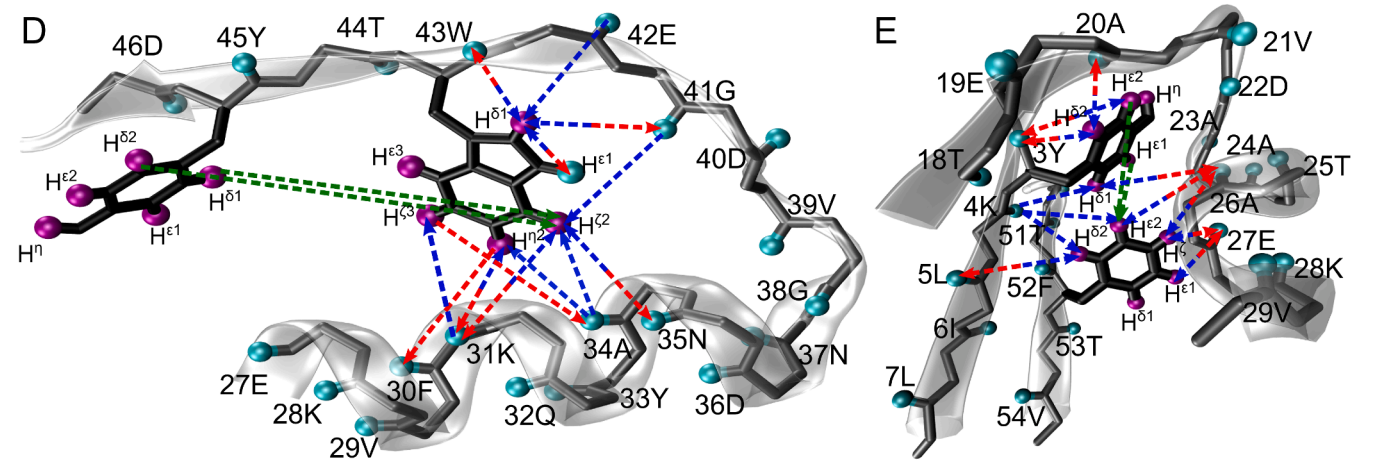

Fig. 5. The F_1-F_3 strips from the (A) (H)N(H^N)(H^C)CH^C (blue), (B) (H)C(H^C)(H^N)NH^N (red) and (C) (H)C(H^C)(H^C)CH^C (green) spectra, showing ^1H–^1H restraints for aromatic residues. The restraints spectra were acquired with the 4X-restraint pulse sequence using 6 ms of BASS-SD mixing. The experimentally observed restraints between α-helix and β-sheets were plotted on the structure of GB1 (PDB: 2QMT) for residues (D) 43W, (E) 3Y and 52F. The arrow indicates $H^N \leftrightarrow H^{aro}$ (blue), $H^{aro} \rightarrow H^N$ (red) and $H^{aro} \rightarrow H^{aro}$ (green) contacts. The H^N atoms are colored cyan and the H^{aro} atoms are colored purple. The H^{aro} atoms are labeled without considering the ring flips. The arrowhead indicates the direction of the transfer. The double-headed arrow indicates that two symmetrical cross-peaks are observed between two spins, and the arrowhead's color shows the transfer's direction. (For interpretation of the references to color in this figure legend, the reader is referred to the web version of this article.)

$C^{aro}(H^{aro})(H^{aro})C^{aro}H^{aro}$ (green) are shown in Fig. 5.

Fig. 5A shows $H^N \rightarrow H^{aro}$ contacts (blue strips). The H^N's of several residues (31K, 34A and 35N) in the α-helix show contact with aromatic protons ($H^{\zeta 2}$, $H^{\zeta 3}$ and $H^{\eta 2}$) of 43W, located in the β3 strand. The 43W ($H^{\delta 1}$) also shows contacts with neighboring residues (42E and 41G). Most of these contacts observed between 43W and other residues are 4–5 Å away. Similarly, the H^N's of residues in the α-helix show contact with residues 3Y and 52F present in the β1 and β4 strands, respectively. 26A and 27E H^N's show contact with 52F ($H^{\varepsilon 1/\varepsilon 2}$ and H^{ζ}). The high-resolution X-ray diffraction structure shows the distance between 52F aromatic protons and 27E and 26A H^N's range from 2.9 Å to 5.2 Å. 52F also shows contact with 4K and 5L in the β1 strand. The residue 3Y shows contact with residues 26A and 20A present in the α-helix and turn region, respectively. In Fig. 5B, the red ($H^{aro} \rightarrow H^N$) strips show most contacts observed in the blue ($H^N \rightarrow H^{aro}$) spectrum but in the opposite direction. These contacts are plotted on the GB1 structure (PDB: 2QMT) and are color-coded as blue in Fig. 5D and E. The arrowhead color denotes the color of the spectrum in which the cross-peak is present. Double-headed arrows with red and blue colors depict the contacts between $H^{aro} \rightarrow H^N$ and $H^N \rightarrow H^{aro}$. The H^{aro}-H^{aro} spectrum (green) in Fig. 5C mostly has intra-residue cross-peaks. Two inter-residue contacts between 52F and 3Y($H^{\varepsilon 1/\varepsilon 2}$) and 43W($H^{\zeta 2}$)-45Y($H^{\delta 1/\delta 2}$) are visible in the spectrum. The observed 43W($H^{\zeta 2}$)-45Y($H^{\delta 1/\delta 2}$) contact (green dotted lines in Fig. 5) corresponds to a distance of about 10.6 Å in the crystal structure (PDB: 2QMT).

The two restraints spectra (RFDR and BASS-SD mixing) generate an exhaustive set of H^N-H^{aro}, H^{aro}–H^N and H^{aro}-H^C restraints. The two spectra demonstrate that RFDR is suited to map out H^C–H^{aro} restraints, where H^C represents aliphatic side-chain protons. In contrast, BASS-SD is suited to observe symmetrical long-range H^N-H^{aro} and H^{aro}-H^N restraints. The RFDR spectra should be acquired by folding $^{13}C^{aro}$ peaks to avoid two dimensions with large ^{13}C spectral widths. In contrast, the BASS-SD recoupled experiment is designed only to evolve $^{13}C^{aro}$ resonances and requires lesser spectral width, thereby reducing the experimental time.

Conclusion

To conclude, the approach proposed in this study functions as an aromatic residue filtering sequence and can be used to identify backbone atoms of aromatic residues in the 2D NH^N and 2D $C^{\alpha}H^{\alpha}$ heteronuclear correlation spectra. The optimized $^{13}C^{aro} \rightarrow {}^{13}C^{\alpha}$ transfer via the TOBSY block links aromatic spins to the backbone atoms for assigning side-chain aromatic spins. The proposed pulse sequence allows the simultaneous acquisition of $(H)C^{aro}NH^N$-TOBSY and $(H)C^{aro}CH^C$-TOBSY spectra in a single experiment. In combination with backbone assignment experiments, the $(H)C^{aro}NH^N$-TOBSY spectrum assists in assigning $^{13}C^{aro}$ spins, while the $(H)C^{aro}CH^C$-TOBSY spectrum assists in assigning $^{1}H^{aro}$ spins in fully protonated proteins. RFDR and BASS-SD recoupling, in combination with the 4X-restraint pulse sequence, generate an extensive set of distance restraints involving aromatic side-chain protons. RFDR is particularly suited for establishing $H^{aro} \leftrightarrow H^C$ contacts, while BASS-SD is better for identifying $H^N \leftrightarrow H^{aro}$ contacts. In the case of GB1, the RFDR and BASS-SD restraints provide important contacts between residues in the hydrophobic core of the protein. The assignment of aromatic side-chain spins in this study allows characterizing of aromatic amino acids in fully protonated samples by ssNMR. In larger proteins with more aromatic residues, additional 3D $H(C^{aro})NH^N$-TOBSY and $H(C^{aro})CH^C$-TOBSY spectra or 4D $HC^{aro}NH^N$-TOBSY and $HC^{aro}CH^C$-TOBSY spectra might be required to assign all aromatic residues unambiguously.

Method and materials

The experiments were recorded on a 700 MHz Avance III spectrometer using the 0.7 mm HCN probe. All the experiments were recorded on U-[^{13}C,^{15}N]-GB1 microcrystals at MAS frequency of 95–100 kHz at a probe temperature of 250 K. The chemical shift values and experimental details of rf fields, mixing times and offsets are mentioned in the Supplementary information (Tables S1–S6). rCW^{ApA} decoupling was used for ^{1}H decoupling (~19 kHz) and WALTZ-16 decoupling was used to decouple ^{13}C (~10 kHz) and ^{15}N (~4 kHz) during the ^{1}H acquisition. The solvent suppression was performed using either the MISSISSIPPI or the SLAP sequences. The spectra were processed in Topspin and analyzed in CCPN software (Stevens et al., 2011).

The pulse program for side-chain assignment acquires two spectra $(H)C^{aro}CH^C$-TOBSY and $(H)C^{aro}NH^N$-TOBSY, in a single experiment. The pulse program separately stores H^C- and H^N-detected FIDs as odd and even points along the t_1 dimension. The individual $(H)C^{aro}CH^C$-TOBSY and $(H)C^{aro}NH^N$-TOBSY spectra are obtained by splitting the odd and even FIDs using the "split" command in the topspin 3.5.7. The 4X-restraint pulse sequence and script for splitting and combining FIDs resulting in spectra encoding four different types of restraints have been previously reported (Ahlawat et al., 2022b).

CRediT authorship contribution statement

Sahil Ahlawat: Conceptualization, Data curation, Investigation, Writing – original draft, Writing – review & editing. **Subbarao Mohana Venkata Mopidevi:** Software, Investigation, Data curation, Writing – review & editing. **Pravin P. Taware:** Investigation, Resources. **Sreejith Raran-Kurussi:** Resources. **Kaustubh R. Mote:** Methodology, Data curation, Writing – review & editing. **Vipin Agarwal:** Conceptualization, Resources, Supervision, Funding acquisition, Methodology, Writing – review & editing.

Declaration of Competing Interest

The authors declare that they have no known competing financial interests or personal relationships that could have appeared to influence the work reported in this paper.

Data availability

Data will be made available on request.

Acknowledgments

We would like to acknowledge Dr. Krishna Rao and the TIFR National Facility of High Field NMR at TIFR Hyderabad for technical assistance and measurement time, respectively. This work is supported by the Department of Atomic Energy, Government of India (GOI), under Project Identification No. RTI 4007 and Department of Biotechnology (GOI) under the grant number BT/INF/22/SP42684/2021.

Appendix A. Supplementary data

Supplementary data to this article can be found online at https://doi.org/10.1016/j.yjsbx.2022.100082.

References

Agarwal, V., Penzel, S., Szekely, K., Cadalbert, R., Testori, E., Oss, A., Past, J., Samoson, A., Ernst, M., Böckmann, A., Meier, B.H., 2014. De novo 3D structure determination from sub-milligram protein samples by solid-state 100 kHz MAS NMR spectroscopy. Angew. Chem. Int. Ed. Engl. 53, 12253–12256. https://doi.org/10.1002/anie.201405730.

Agarwal, V., Reif, B., 2008. Residual methyl protonation in perdeuterated proteins for multi-dimensional correlation experiments in MAS solid-state NMR spectroscopy. J. Magn. Reson. 194, 16–24. https://doi.org/10.1016/j.jmr.2008.05.021.

Ahlawat, S., Mote, K.R., Lakomek, N.-A., Agarwal, V., 2022a. Solid-State NMR: Methods for Biological Solids. Chem. Rev. 122, 9643–9737. https://doi.org/10.1021/acs.chemrev.1c00852.

Ahlawat, S., Mote, K.R., Raran-Kurussi, S., Agarwal, V., 2022b. Mechanism of selective polarization exchange amongst chemically similar and distinct protons during weak

rf irradiation at fast magic angle spinning. J. Magn. Reson. 340, 107236 https://doi.org/10.1016/j.jmr.2022.107236.
Andreas, L.B., Stanek, J., Le Marchand, T., Bertarello, A., Cala-De Paepe, D., Lalli, D., Krejčíková, M., Doyen, C., Öster, C., Knott, B., Wegner, S., Engelke, F., Felli, I.C., Pierattelli, R., Dixon, N.E., Emsley, L., Herrmann, T., Pintacuda, G., 2015. Protein residue linking in a single spectrum for magic-angle spinning NMR assignment. J. Biomol. NMR 62, 253–261. https://doi.org/10.1007/s10858-015-9956-1.
Andreas, L.B., Jaudzems, K., Stanek, J., Lalli, D., Bertarello, A., Le Marchand, T., Cala-De Paepe, D., Kotelovica, S., Akopjana, I., Knott, B., Wegner, S., Engelke, F., Lesage, A., Emsley, L., Tars, K., Herrmann, T., Pintacuda, G., 2016. Structure of fully protonated proteins by proton-detected magic-angle spinning NMR. Proc. Natl. Acad. Sci. U.S.A. 113, 9187–9192. https://doi.org/10.1073/pnas.1602248113.
Bak, M., Rasmussen, J.T., Nielsen, N.C., 2000. SIMPSON: A General Simulation Program for Solid-State NMR Spectroscopy. J. Magn. Reson. 147, 296–330. https://doi.org/10.1006/jmre.2000.2179.
Baldus, M., Meier, B.H., 1996. Total correlation spectroscopy in the solid state. The use of scalar couplings to determine the through-bond connectivity. J. Magn. Reson. A 121, 65–69. https://doi.org/10.1006/jmra.1996.0137.
Banigan, J.R., Traaseth, N.J., 2012. Utilizing afterglow magnetization from cross-polarization magic-angle-spinning solid-state NMR spectroscopy to obtain simultaneous heteronuclear multidimensional spectra. J. Phys. Chem. B 116, 7138–7144. https://doi.org/10.1021/jp303269m.
Bennett, A.E., Griffin, R.G., Ok, J.H., Vega, S., 1992. Chemical shift correlation spectroscopy in rotating solids: Radio frequency-driven dipolar recoupling and longitudinal exchange. J. Chem. Phys. 96, 8624–8625. https://doi.org/10.1063/1.462267.
Bjerring, M., Paaske, B., Oschkinat, H., Akbey, Ü., Nielsen, N.C., 2012. Rapid solid-state NMR of deuterated proteins by interleaved cross-polarization from ^{1}H and ^{2}H nuclei. J. Magn. Reson. 214, 324–328. https://doi.org/10.1016/j.jmr.2011.10.020.
Cavanagh, J., Skelton, N.J., Fairbrother, W.J., Rance, M., Palmer, A.G., 2010. Protein NMR Spectroscopy: Principles and Practice. Elsevier Science.
Chen, L., Olsen, R.A., Elliott, D.W., Boettcher, J.M., Zhou, D.H., Rienstra, C.M., Mueller, L.J., 2006. Constant-time through-bond 13C correlation spectroscopy for assigning protein resonances with solid-state NMR spectroscopy. J. Am. Chem. Soc. 128, 9992–9993. https://doi.org/10.1021/ja062347t.
Daskalov, A., Martinez, D., Coustou, V., El Mammeri, N., Berbon, M., Andreas, L.B., Bardiaux, B., Stanek, J., Noubhani, A., Kauffmann, B., Wall, J.S., Pintacuda, G., Saupe, S.J., Habenstein, B., Loquet, A., 2021. Structural and molecular basis of cross-seeding barriers in amyloids. Proc Natl Acad Sci U S A 118 (1), e2014085118. https://doi.org/10.1073/pnas.2014085118.
Duong, N.T., Raran-Kurussi, S., Nishiyama, Y., Agarwal, V., 2018. Quantitative ^{1}H-^{1}H Distances in Protonated Solids by Frequency-Selective Recoupling at Fast Magic Angle Spinning NMR. J Phys Chem Lett 9, 5948–5954. https://doi.org/10.1021/acs.jpclett.8b02189.
Duong, N.T., Raran-Kurussi, S., Nishiyama, Y., Agarwal, V., 2020. Can proton-proton recoupling in fully protonated solids provide quantitative, selective and efficient polarization transfer? J. Magn. Reson. 317, 106777 https://doi.org/10.1016/j.jmr.2020.106777.
Emsley, L., Bodenhausen, G., 1992. Optimization of shaped selective pulses for NMR using a quaternion description of their overall propagators. J. Magn. Reson. 1969 (97), 135–148. https://doi.org/10.1016/0022-2364(92)90242-Y.
Fraga, H., Arnaud, C.-A., Gauto, D.F., Audin, M., Kurauskas, V., Macek, P., Krichel, C., Guan, J.-Y., Boisbouvier, J., Sprangers, R., Breyton, C., Schanda, P., 2017. Solid-State NMR H-N-(C)-H and H-N-C-C 3D/4D Correlation Experiments for Resonance Assignment of Large Proteins. ChemPhysChem 18, 2697–2703. https://doi.org/10.1002/cphc.201700572.
Gauto, D.F., Lebedenko, O.O., Becker, L.M., Ayala, I., Lichtenecker, R., Skrynnikov, N.R., Schanda, P., 2022. Aromatic ring flips in differently packed protein crystals: MAS NMR and MD studies of 3 ubiquitin lattices. bioRxiv 2022.07.07.499110. 10.1101/2022.07.07.499110.
Gauto, D.F., Macek, P., Barducci, A., Fraga, H., Hessel, A., Terauchi, T., Gajan, D., Miyanoiri, Y., Boisbouvier, J., Lichtenecker, R., Kainosho, M., Schanda, P., 2019. Aromatic Ring Dynamics, Thermal Activation, and Transient Conformations of a 468 kDa Enzyme by Specific 1H–13C Labeling and Fast Magic-Angle Spinning NMR. J. Am. Chem. Soc. 141, 11183–11195. https://doi.org/10.1021/jacs.9b04219.
Ghassemi, N., Poulhazan, A., Deligey, F., Mentink-Vigier, F., Marcotte, I., Wang, T., 2022. Solid-State NMR Investigations of Extracellular Matrixes and Cell Walls of Algae, Bacteria, Fungi, and Plants. Chem. Rev. 122, 10036–10086. https://doi.org/10.1021/acs.chemrev.1c00669.
Ghosh, M., Rienstra, C.M., 2017. 1H-Detected REDOR with Fast Magic-Angle Spinning of a Deuterated Protein. J. Phys. Chem. B 121, 8503–8511. https://doi.org/10.1021/acs.jpcb.7b07313.
Gopinath, T., Veglia, G., 2012a. 3D DUMAS: simultaneous acquisition of three-dimensional magic angle spinning solid-state NMR experiments of proteins. J. Magn. Reson. 220, 79–84. https://doi.org/10.1016/j.jmr.2012.04.006.
Gopinath, T., Veglia, G., 2012b. Dual acquisition magic-angle spinning solid-state NMR-spectroscopy: simultaneous acquisition of multidimensional spectra of biomacromolecules. Angew. Chem. Int. Ed. Engl. 51, 2731–2735. https://doi.org/10.1002/anie.201108132.
Hardy, E.H., Verel, R., Meier, B.H., 2001. Fast MAS Total Through-Bond Correlation Spectroscopy. J. Magn. Reson. 148, 459–464. https://doi.org/10.1006/jmre.2000.2258.
Hardy, E.H., Detken, A., Meier, B.H., 2003. Fast-MAS total through-bond correlation spectroscopy using adiabatic pulses. J. Magn. Reson. 165, 208–218. https://doi.org/10.1016/j.jmr.2003.08.003.
Herbst, C., Riedel, K., Ihle, Y., Leppert, J., Ohlenschläger, O., Görlach, M., Ramachandran, R., 2008. MAS solid-state NMR of RNAs with multiple receivers. J. Biomol. NMR 41, 121–125. https://doi.org/10.1007/s10858-008-9247-1.
Higman, V.A., 2018. Solid-state MAS NMR resonance assignment methods for proteins. Prog. Nucl. Magn. Reson. Spectrosc. 106–107, 37–65. https://doi.org/10.1016/j.pnmrs.2018.04.002.
Ivchenko, N., Hughes, C.E., Levitt, M.H., 2003. Multiplex phase cycling. J. Magn. Reson. 160, 52–58. https://doi.org/10.1016/s1090-7807(02)00108-8.
Jain, M.G., Lalli, D., Stanek, J., Gowda, C., Prakash, S., Schwarzer, T.S., Schubeis, T., Castiglione, K., Andreas, L.B., Madhu, P.K., Pintacuda, G., Agarwal, V., 2017. Selective 1H–1H Distance Restraints in Fully Protonated Proteins by Very Fast Magic-Angle Spinning Solid-State NMR. J. Phys. Chem. Lett. 8, 2399–2405. https://doi.org/10.1021/acs.jpclett.7b00983.
Kainosho, M., Torizawa, T., Iwashita, Y., Terauchi, T., Mei Ono, A., Güntert, P., 2006. Optimal isotope labelling for NMR protein structure determinations. Nature 440, 52–57. https://doi.org/10.1038/nature04525.
Klein, A., Rovó, P., Sakhrani, V.V., Wang, Y., Holmes, J.B., Liu, V., Skowronek, P., Kukuk, L., Vasa, S.K., Güntert, P., Mueller, L.J., Linser, R., 2022a. Atomic-resolution chemical characterization of (2x)72-kDa tryptophan synthase via four- and five-dimensional 1H-detected solid-state NMR. Proc. Natl. Acad. Sci. U.S.A. 119 https://doi.org/10.1073/pnas.2114690119.
Klein, A., Vasa, S.K., Söldner, B., Grohe, K., Linser, R., 2022b. Unambiguous Side-Chain Assignments for Solid-State NMR Structure Elucidation of Nondeuterated Proteins via a Combined 5D/4D Side-Chain-to-Backbone Experiment. J. Phys. Chem. Lett. 13, 1644–1651. https://doi.org/10.1021/acs.jpclett.1c04075.
Kulminskaya, N., Vasa, S.K., Giller, K., Becker, S., Linser, R., 2015. Asynchronous through-bond homonuclear isotropic mixing: application to carbon-carbon transfer in perdeuterated proteins under MAS. J. Biomol. NMR 63, 245–253. https://doi.org/10.1007/s10858-015-9980-1.
Kulminskaya, N., Vasa, S.K., Giller, K., Becker, S., Kwan, A., Sunde, M., Linser, R., 2016. Access to side-chain carbon information in deuterated solids under fast MAS through non-rotor-synchronized mixing. Chem. Commun. (Camb.) 52, 268–271. https://doi.org/10.1039/c5cc07345f.
Lakomek, N.-A., Frey, L., Bibow, S., Böckmann, A., Riek, R., Meier, B.H., 2017. Proton-Detected NMR Spectroscopy of Nanodisc-Embedded Membrane Proteins: MAS Solid-State vs Solution-State Methods. J. Phys. Chem. B 121, 7671–7680. https://doi.org/10.1021/acs.jpcb.7b06944.
Le Marchand, T., Schubeis, T., Bonaccorsi, M., Paluch, P., Lalli, D., Pell, A.J., Andreas, L.B., Jaudzems, K., Stanek, J., Pintacuda, G., 2022. 1H-Detected Biomolecular NMR under Fast Magic-Angle Spinning. Chem. Rev. 122, 9943–10018. https://doi.org/10.1021/acs.chemrev.1c00918.
Lecoq, L., Fogeron, M.-L., Meier, B.H., Nassal, M., Böckmann, A., 2020. Solid-State NMR for Studying the Structure and Dynamics of Viral Assemblies. Viruses 12. https://doi.org/10.3390/v12101069, 1069–1026.
Lecoq, L., Schledorn, M., Wang, S., Smith-Penzel, S., Malär, A.A., Callon, M., Nassal, M., Meier, B.H., Böckmann, A., 2019. 100 kHz MAS Proton-Detected NMR Spectroscopy of Hepatitis B Virus Capsids. Front Mol Biosci 6. https://doi.org/10.3389/fmolb.2019.00058, 58–10.
Lesage, A., Auger, C., Stefano Caldarelli, A., Emsley, L., 1997. Determination of Through-Bond Carbon−Carbon Connectivities in Solid-State NMR Using the INADEQUATE Experiment. J. Am. Chem. Soc. 119, 7867–7868. https://doi.org/10.1021/ja971089k.
Lesage, A., Bardet, M., Emsley, L., 1999. Through-bond carbon− carbon connectivities in disordered solids by NMR. J. Am. Chem. Soc. 121, 10987–10993. https://doi.org/10.1021/ja992272b.
Levitt, M., 2007. Symmetry-Based Pulse Sequences in Magic-Angle Spinning Solid-State NMR: Solid-State NMR Studies of Biopolymers. Wiley.
Loening, N.M., Bjerring, M., Nielsen, N.C., Oschkinat, H., 2012. A comparison of NCO and NCA transfer methods for biological solid-state NMR spectroscopy. J. Magn. Reson. 214, 81–90. https://doi.org/10.1016/j.jmr.2011.10.012.
Manolikas, T., Herrmann, T., Meier, B.H., 2008. Protein structure determination from 13C spin-diffusion solid-state NMR spectroscopy. J. Am. Chem. Soc. 130, 3959–3966. https://doi.org/10.1021/ja078039s.
Matsunaga, T., Okabe, R., Ishii, Y., 2021. Efficient solvent suppression with adiabatic inversion for 1H-detected solid-state NMR. J Biomol NMR 75, 365–370. https://doi.org/10.1007/s10858-021-00384-8.
Mueller, L.J., Elliott, D.W., Kim, K.-C., Reed, C.A., Boyd, P.D.W., 2002. Establishing through-bond connectivity in solids with NMR: structure and dynamics in HC(60)(+). J. Am. Chem. Soc. 124, 9360–9361. https://doi.org/10.1021/ja0266619.
Nielsen, A.B., Jain, S., Ernst, M., Meier, B.H., Nielsen, N.C., 2013. Adiabatic Rotor-Echo-Short-Pulse-Irradiation mediated cross-polarization. J. Magn. Reson. 237, 147–151. https://doi.org/10.1016/j.jmr.2013.09.002.
Nimerovsky, E., Najbauer, E.E., Movellan, K.T., Xue, K., Becker, S., Andreas, L.B., 2022. Modest Offset Difference Internuclear Selective Transfer via Homonuclear Dipolar Coupling. J Phys Chem Lett 13, 1540–1546. https://doi.org/10.1021/acs.jpclett.1c03871.
Olsen, R.A., Struppe, J., Elliott, D.W., Thomas, R.J., Mueller, L.J., 2003. Through-bond 13C–13C correlation at the natural abundance level: refining dynamic regions in the crystal structure of vitamin-D3 with solid-state NMR. J. Am. Chem. Soc. 125, 11784–11785. https://doi.org/10.1021/ja036655s.
Paluch, P., Augustyniak, R., Org, M.-L., Vanatalu, K., Kaldma, A., Samoson, A., Stanek, J., 2022. NMR Assignment of Methyl Groups in Immobilized Proteins Using Multiple-Bond 13C Homonuclear Transfers, Proton Detection, and Very Fast MAS. Front. Mol. Biosci. 9, 828785 https://doi.org/10.3389/fmolb.2022.828785.
Penzel, S., Smith, A.A., Agarwal, V., Hunkeler, A., Org, M.-L., Samoson, A., Böckmann, A., Ernst, M., Meier, B.H., 2015. Protein resonance assignment at MAS

frequencies approaching 100 kHz: a quantitative comparison of J-coupling and dipolar-coupling-based transfer methods. J. Biomol. NMR 63, 165–186. https://doi.org/10.1007/s10858-015-9975-y.

Potnuru, L.R., Duong, N.T., Ahlawat, S., Raran-Kurussi, S., Ernst, M., Nishiyama, Y., Agarwal, V., 2020. Accuracy of ^{1}H-^{1}H distances measured using frequency selective recoupling and fast magic-angle spinning. J Chem Phys 153, 084202. https://doi.org/10.1063/5.0019717.

Russell, R.W., Fritz, M.P., Kraus, J., Quinn, C.M., Polenova, T., Gronenborn, A.M., 2019. Accuracy and precision of protein structures determined by magic angle spinning NMR spectroscopy: for some 'with a little help from a friend'. J. Biomol. NMR 73, 333–346. https://doi.org/10.1007/s10858-019-00233-9.

Schubeis, T., Le Marchand, T., Daday, C., Kopec, W., Tekwani Movellan, K., Stanek, J., Schwarzer, T.S., Castiglione, K., de Groot, B.L., Pintacuda, G., Andreas, L.B., 2020. A β-barrel for oil transport through lipid membranes: Dynamic NMR structures of AlkL. Proc. Natl. Acad. Sci. U.S.A. 117, 21014–21021. https://doi.org/10.1073/pnas.2002598117.

Schubeis, T., Stanek, J., Pintacuda, G., 2021. Backbone assignment of crystalline E. coli maltose binding protein. Biomol. NMR Assign. 15, 317–322. https://doi.org/10.1007/s12104-021-10023-w.

Sharma, K., Madhu, P.K., Agarwal, V., Mote, K.R., 2020. Simultaneous recording of intra- and inter-residue linking experiments for backbone assignments in proteins at MAS frequencies higher than 60 kHz. J. Biomol. NMR 74, 229–237. https://doi.org/10.1007/s10858-019-00292-y.

Shcherbakov, A.A., Hong, M., 2018. Rapid measurement of long-range distances in proteins by multidimensional 13C–19F REDOR NMR under fast magic-angle spinning. J. Biomol. NMR 71, 31–43. https://doi.org/10.1007/s10858-018-0187-0.

Shi, X., Rienstra, C.M., 2016. Site-Specific Internal Motions in GB1 Protein Microcrystals Revealed by 3D ^{2}H–^{13}C-^{13}C Solid-State NMR Spectroscopy. J. Am. Chem. Soc. 138, 4105–4119. https://doi.org/10.1021/jacs.5b12974.

Stanek, J., Andreas, L.B., Jaudzems, K., Cala, D., Lalli, D., Bertarello, A., Schubeis, T., Akopjana, I., Kotelovica, S., Tars, K., Pica, A., Leone, S., Picone, D., Xu, Z.-Q., Dixon, N.E., Martinez, D., Berbon, M., Mammeri, El, N., Noubhani, A., Saupe, S., Habenstein, B., Loquet, A., Pintacuda, G., 2016. NMR Spectroscopic Assignment of Backbone and Side-Chain Protons in Fully Protonated Proteins: Microcrystals, Sedimented Assemblies, and Amyloid Fibrils. Angew. Chem. Int. Ed. Engl. 55, 15504–15509. 10.1002/anie.201607084.

Stanek, J., Schubeis, T., Paluch, P., Güntert, P., Andreas, L.B., Pintacuda, G., 2020. Automated backbone NMR resonance assignment of large proteins using redundant linking from a single simultaneous acquisition. J. Am. Chem. Soc. 142, jacs.0c00251–5799. 10.1021/jacs.0c00251.

Stevens, T.J., Fogh, R.H., Boucher, W., Higman, V.A., Eisenmenger, F., Bardiaux, B., van Rossum, B.-J., Oschkinat, H., Laue, E.D., 2011. A software framework for analysing solid-state MAS NMR data. J. Biomol. NMR 51, 437–447. https://doi.org/10.1007/s10858-011-9569-2.

Takeda, K., Kusakabe, Y., Noda, Y., Fukuchi, M., Takegoshi, K., 2012. Homo- and heteronuclear two-dimensional covariance solid-state NMR spectroscopy with a dual-receiver system. Phys. Chem. Chem. Phys. 14, 9715–9721. https://doi.org/10.1039/c2cp41191a.

Tan, K.O., Agarwal, V., Lakomek, N.-A., Penzel, S., Meier, B.H., Ernst, M., 2018. Efficient low-power TOBSY sequences for fast MAS. Solid State Nucl. Magn. Reson. 89, 27–34. https://doi.org/10.1016/j.ssnmr.2017.11.003.

Teilum, K., Brath, U., Lundström, P., Akke, M., 2006. Biosynthetic 13C labeling of aromatic side chains in proteins for NMR relaxation measurements. J. Am. Chem. Soc. 128, 2506–2507. https://doi.org/10.1021/ja055660o.

Tolchard, J., Pandey, M.K., Berbon, M., Noubhani, A., Saupe, S.J., Nishiyama, Y., Habenstein, B., Loquet, A., 2018. Detection of side-chain proton resonances of fully protonated biosolids in nano-litre volumes by magic angle spinning solid-state NMR. J. Biomol. NMR 70, 177–185. https://doi.org/10.1007/s10858-018-0168-3.

Torizawa, T., Ono, A.M., Terauchi, T., Kainosho, M., 2005. NMR assignment methods for the aromatic ring resonances of phenylalanine and tyrosine residues in proteins. J. Am. Chem. Soc. 127, 12620–12626. https://doi.org/10.1021/ja051386m.

Tošner, Z., Andersen, R., Stevensson, B., Edén, M., Nielsen, N.C., Vosegaard, T., 2014. Computer-intensive simulation of solid-state NMR experiments using SIMPSON. J. Magn. Reson. 246, 79–93. https://doi.org/10.1016/j.jmr.2014.07.002.

Verel, R., Ernst, M., Meier, B.H., 2001. Adiabatic dipolar recoupling in solid-state NMR: the DREAM scheme. J. Magn. Reson. 150, 81–99. https://doi.org/10.1006/jmre.2001.2310.

Wi, S., Frydman, L., 2020. An Efficient, Robust New Scheme for Establishing Broadband Homonuclear Correlations in Biomolecular Solid State NMR. ChemPhysChem 21, 284–294. https://doi.org/10.1002/cphc.201901071.

Xiang, S., Grohe, K., Rovó, P., Vasa, S.K., Giller, K., Becker, S., Linser, R., 2015. Sequential backbone assignment based on dipolar amide-to-amide correlation experiments. J. Biomol. NMR 62, 303–311. https://doi.org/10.1007/s10858-015-9945-4.

Zhang, Z., Oss, A., Org, M.-L., Samoson, A., Li, M., Tan, H., Su, Y., Yang, J., 2020. Selectively Enhanced ^{1}H–^{1}H Correlations in Proton-Detected Solid-State NMR under Ultrafast MAS Conditions. J. Phys. Chem. Lett. 11, 8077–8083. https://doi.org/10.1021/acs.jpclett.0c02412.